Atmósfera 37, 383-399 (2023)
https://doi.org/10.20937/ATM.53156

Experimental downslope gravity currents over a synthetic topography

Andrea BURGOS-CUEVAS[1,3]*, Angel RUIZ-ANGULO[2], Karina RAMOS-MUSALEM[3], Carlos PALACIOS-MORALES[4] and Cruz GARCÍA-MOLINA[5]

[1] *Institute for Geophysics and Meteorology, University of Cologne, Cologne, 50969, Germany.*
[2] *Institute of Earth Sciences, University of Iceland, Reykjavik, 101, Iceland.*
[3] *Instituto de Ciencias de la Atmósfera y Cambio Climático, Universidad Nacional Autónoma de México, Ciudad de México City, 04510, México.*
[4] *Facultad de Ingeniería, Universidad Nacional Autónoma de México, Ciudad de México 04510, México.*
[5] *Univ. Grenoble Alpes, IRD, CNRS, Grenoble INP, IGE, 38000 Grenoble, France, Institute of Engineering and Management Univ. Grenoble Alpes.*
*Corresponding author: aburgosc@uni-koeln.de

Received: December 23, 2021; accepted: May 11, 2022

RESUMEN

Se estudian corrientes de gravedad producidas en el laboratorio mediante una configuración de compuerta tipo lock-release mientras se desplazan pendiente abajo en una topografía variable. Se pretende emular y estudiar la dinámica de flujos similares a los vientos térmicamente desarrollados en las laderas de las montañas, que se propagan interaccionando con la superficie topográficamente compleja. Los procesos de mezcla entre las corrientes de gravedad y sus alrededores son estudiados mediante Velocimetría por Imágenes de Partículas (PIV, por sus siglas en inglés) y se cuantifican las intrusiones turbulentas conocidas como entrainment. Se muestra que la magnitud del coeficiente de entrainment incrementa conforme aumenta también la rugosidad de la superficie de la pendiente. Además, las visualizaciones mediante la técnica *shadowgraph* cualitativamente reproducen este comportamiento. Por último, se utilizan los campos de velocidad para estimar campos de presión y con ellos series de tiempo de presión en estaciones sintéticas a lo largo de la pendiente. Se muestra que la llegada de la corriente de gravedad a las estaciones en la pendiente puede ser detectada en las series de presión. Este último resultado puede ser útil para detectar corrientes de gravedad atmosféricas utilizando solamente mediciones de presión en superficie.

ABSTRACT

Experimental lock-release gravity currents are investigated as they propagate downslope over varying synthetic topography. We emulate and investigate the dynamics of thermally driven winds that propagate downslope while interacting with the roughness of a complex topographic surface. The mixing processes between the gravity currents and their surroundings are studied with Particle Image Velocimetry (PIV), and entrainment is quantified. The magnitude of the entrainment coefficient is shown to increase as the roughness of the slope increases. Shadowgraph visualizations qualitatively reproduce this behavior. Finally, pressure fields are estimated from velocity fields, and pressure time series are obtained over synthetic stations along the topographic surface. The arrival of gravity currents is shown to be detected in the pressure time series. This last result may help detect atmospheric gravity currents using only surface pressure measurements.

Keywords: Gravity currents, entrainment, pressure time series, topographic slope.

1. Introduction

Gravity currents are flows that develop when there is a horizontal density gradient in the presence of a gravitational field. This density difference causes the heavier fluid (gravity current) to intrude beneath the lighter one (ambient fluid) with a mainly horizontal

displacement (Huppert and Simpson, 1980; Linden, 2011). Gravity currents appear in a variety of natural and man-made phenomena at different scales (Simpson, 1999; Ungarish, 2009; Wu and Dai, 2020). Examples include thermally driven winds in the hillside of the mountains, sea breezes, oceanic fronts, squall lines in thunderstorms, pyroclastic flows, and the cold air from outside entering a warm house when the door is opened.

When a fluid is in a gravitational field, buoyancy forces appear whenever there are density variations. Particularly, when density varies in the horizontal direction, a gravity current (GC) will always result (Linden, 2012). The GC acquires an acceleration called reduced gravity, g', which depends on the density contrast between the GC (with density ρc) and the ambient fluid around it (with density ρa),

$$g' = \frac{g\left(\rho_c - \rho_a\right)}{\rho_a} = g\Gamma \tag{1}$$

where $\Gamma = \frac{\rho_c - \rho_a}{\rho_a}$ and $g = 9.8ms^{-2}$. As a GC propagates, inertial and gravitational forces are present, and the balance between them is represented by the Froude number (Fr) (Benjamin, 1968), related to the dimensionless velocity of a GC:

$$Fr = \frac{\overline{u}}{g'h}, \tag{2}$$

where $\overline{u}$ is the mean velocity and h is the height of the GC. Additionally, the Reynolds number,

$$Re = \frac{\overline{u}L}{\nu}, \tag{3}$$

where L is a characteristic length and v is the kinematic viscosity, a key parameter for studying turbulent flows. Finally, when investigating the mixing between the gravity currents and the ambient fluid, the Richardson number is crucial. This dimensionless parameter expresses the ratio of the buoyancy term to the flow shear term, which can be estimated as:

$$Ri = \frac{g}{\rho}\frac{\partial\rho/\partial z}{(\partial u/\partial z)^2} \tag{4}$$

where u is the velocity of the flow and ρ its density. The Richardson number in gravity currents is further analyzed in this study because the entrainment, E, depends on this dimensionless parameter (Ellison and Turner, 1959). Because they influence the dynamics of the atmosphere and the ocean and even have industrial applications (Fleischmann et al., 1994), gravity currents have been the subject of numerous studies. Many of them have focused on experimental gravity currents propagating over smooth flat bottoms or smooth slopes using the typical lock-exchange configuration (Mitsudera and Baines, 1992; Simpson, 1999; Reuten et al., 2010; Linden, 2012; Shin et al., 2004; Adduce et al., 2012; Lowe et al., 2002; Ungarish, 2016; Balasubramanian and Zhong, 2018; Mukherjee and Balasubramanian, 2020, 2021). Nevertheless, in nature, gravity currents propagate over complex topographies. In particular, in this study, we are interested in gravity currents that may simulate the thermally driven winds propagating over a topographic slope.

There has been a growing interest in understanding the impact of bottom roughness (Nogueira et al., 2013, 2014; Cenedese et al., 2016, 2018; Tanino et al., 2005; Zhang and Nepf, 2008; Bhaganagar and Pillalamarri, 2017; Wilson et al., 2017; Jiang and Liu, 2018; Xu et al., 2019; Zhou and Venayagamoorthy, 2020; Maggi et al., 2022) and isolated obstacles (Tokyay and Constantinescu. 2015, de Falco et al. 2021) on gravity current propagation. In particular, the presence of rectangular obstacles was shown to increase entrainment as the GC propagates downstream (Wilson et al., 2017). On the other hand, different bed roughnesses were tested by Nogueira et al. (2013), and they found that diverse granular media play an important role in the current dynamics, mainly because the extra drag at the bed decreases the front velocity (Nogueira et al., 2013). Bottom roughness has been experimentally idealized by different arrangements of rigid cylinders by Cenedese et al. (2016, 2018) and Maggi et al. (2022). The former measured density fields and found entrainment enhancement by different processes depending on the configuration of the cylinders. In contrast, the latter found that the relative height of the cylinders to the gravity current depth controls the structure and propagation speed of the current with higher roughness elements generating strong recirculation areas between cylinders that interact and modify the overlying current. These investigations have shown that idealized topography affects the gravity current profile (Tanino et al., 2005) and the mixing mechanisms (Cenedese et al., 2018). To quantify entrainment, previous authors (Cenedese

and Adduce., 2008; Nogueira et al., 2013; Ottolenghi et al., 2016; Wilson et al., 2017; Ottolenghi et al., 2017; Balasubramanian and Zhong, 2018) have utilized the Morton-Taylor-Turner (MTT) entrainment hypothesis (Ellison and Turner, 1959):

$$E = \frac{w_e}{U} \tag{5}$$

where U is a characteristic velocity and w_e is the entrainment velocity, perpendicular to U. As the GC propagates, the velocity of inflow into the turbulent region can be assumed proportional to the velocity scale of the turbulent layer, and the constant of proportionality is E. Ellison and Turner (1959) estimated E for neutral and traveling downslope jets; they showed that this coefficient ranges between 0.01 and 0.1. Other studies have considered these values for studying gravity currents (Turner, 1986; Princevac et al., 2008; Manins and Sawford, 1979). However, the MTT hypothesis may underestimate the entrainment rate in atmospheric flows (Princevac et al., 2008) because natural flows occur at much higher Reynolds numbers ($\mathrm{Re}\approx10^7$) than the ones in a laboratory tank ($\mathrm{Re}\approx10^3$). Experimental and numerical gravity current studies have extended the range of entrainment values between 10^{-4} and 10^{-1} (Ottolenghi et al., 2016; Cenedese and Adduce, 2008).

To estimate entrainment using equation 5, the velocities U and w_e must be quantified. While it is relatively simple to calculate U, parametrizing the entrainment velocity w_e is not easy. Some authors have evaluated w_e as the flow of ambient fluid crossing the interface between the dense current and the ambient fluid around it per unit area. This idea was proposed by Cenedese and Adduce (2008), and it has been widely implemented to quantify entrainment (Nogueira et al., 2013; Ottolenghi et al., 2016, 2017; Wilson et al., 2017).

The present study investigates a synthetic topography's influence on gravity currents' dynamics. The entrainment coefficient is estimated from the velocity fields, which were measured experimentally using Particle Image Velocimetry (PIV). Utilizing these measured velocity fields, the entrainment is studied by the MTT assumption (equation 5) and with an analysis presented by Princevac et al. (2008), which will be further explained in the Methodology. We are particularly interested in the dependence of ntrainment on bottom topography. To get insight into this dependence, the experimental gravity currents were allowed to propagate over different sections of a topographic surface as similar as possible to a mountain slope near the Valley of Mexico. Additionally, qualitative visualizations are performed to better characterize the flow propagation and the spatial and temporal variations of the mixing. These visualizations illustrate the mixing while gravity currents propagate over the topographic slope.

The particular situation of gravity currents propagating downslope on a topographic surface is of interest in the Valley of Mexico because thermally-driven winds are known to propagate in that region (Doran et al., 1998; Fast and Zhong, 1998). Nevertheless, identifying these flows in the atmosphere is hardly achieved with the velocity fields because those fields are not as easily measured in the valley as they can be measured in a laboratory tank or a numerical simulation. Therefore, we are also interested in finding a dynamic condition to help us identify gravity currents in the atmosphere. We also utilized the measured velocity fields to estimate instantaneous pressure fields and obtain pressure time series over synthetic stations along the topographic surface that is shown in figure 1. These pressure time series allowed us to relate fast variations in the pressure to the arrival of gravity currents to synthetic stations. The measurement of atmospheric pressure in stations around a valley is much simpler and cheaper than the velocity field measurements. Therefore, such a pressure condition may help detect atmospheric gravity currents.

2. Methodology

2.1 Experimental set-up

Experimental lock-release gravity currents are produced in a tank of rectangular cross-section (see figure 2). The density contrasts between the two liquids are created using saline solutions. The resulting densities were measured with an *Anton Paar* densitometer. Each GC develops over a flat section (15 cm long) followed by a slope of 5º. A synthetic topography was printed over an acrylic slab following the "Tláloc" volcano hillside profile. The manufacturing process was possible using a computer numeric control (CNC) machine.

The synthetic topography on the slope is scaled with the one from the "*Tláloc*" volcano near the Valley of Mexico.

Because the horizontal scale is much larger than the vertical scale, we split the entire slope into three sections. We consider eight cases described in Table I. For comparison purposes, the base case is the GC propagating over a flat slope. The rest of the seven cases are performed using a synthetic topography. The entire section is divided into three subsections (Figure 1 b). We explore different combinations of parameters, such as g' and the varying topography over the slope. Firstly, we investigate the propagation of gravity currents with initial $g' = 14$ cm s^{-2} over each of the topographic and flat slope sections. Secondly, we study gravity currents varying g' and propagating over the lower section of the topographic slope. Two smaller and two larger g' than14 cm s^{-2} are considered.

We utilized two different experimental techniques to study the GCs. The first is a simple qualitative visualization with a shadowgraph, and the second uses Particle Image Velocimetry (PIV). The shadowgraph visualization is implemented by displaying a white light source from behind the tank and placing a screen opposite it. A camera then records the pattern of lights and shadows on the screen.

A two-dimensional particle image velocimetry technique or 2D-2C PIV was employed to obtain the velocity fields of the gravity current. Illumination, capturing, and processing equipment were necessary. A Dantec Dynamics System was used to perform the measurements. The illumination system consisted of a doubled pulsed Nd:YAG Litron laser, illuminating the test section from below the tank using special optics that transformed a cylindrical beam into a light sheet. The fluid was previously seeded with neutrally buoyant silver-coated microspheres of glass. A Phantom CMOS Speed Sense M320 camera was used to capture the images and was placed facing perpendicular to the laser sheet. A 40 mm Nikon lens was also employed.

The camera has a resolution of 1920 × 1200 pixels; however, for these experiments, the region of interest was 1858 by 755 pixels. The laser and camera shots were synchronized and controlled by the Dynamic Studio software version 4.0.37 from Danted Dynamics. The velocity vectors were also obtained using this software. An image masking procedure was implemented to isolate the fluid region where vectors were computed. An adaptive cross-correlation algorithm was used to obtain the instantaneous velocity fields. Different criteria and filters were employed to eliminate spurious vectors and improve velocity fields. Typically, 2960 independent vectors were obtained with a sampling frequency of 55 Hz and a spatial resolution of 3.85 mm. The region of interest corresponds approximately to an area of 325.6 × 132.4 mm.

2.2 Entrainment estimations

To use the MTT assumption (equation 5) for the estimation of E, we consider the analysis presented by Manins and Sawford (1979) and Princevac et al. (2008). The Princevac analysis considers a downslope gravity current with a transformation of the coordinate system (s,n) such that s and n are the tangent and normal directions to the slope, respectively.

Table I. Summary of the main parameters for the eight experimental runs. Different density contrasts, Γ (and therefore $g's$), are utilized. Additionally, gravity currents propagating over different bottoms are studied. The variables U, Re_u, Fr_u, Ri and E in this table correspond to the mean values for each run; Γ and g' correspond to the initial values, before the lock was released.

Run	Bottom	Γ	g'(cms^{-2})	U(cms^{-1})	Re_u	Fr_u	Ri	E(mean)
F01	flat (no topography)	0.014	14	6.23	18615	1.36	0.34	0.0406
TU01	upper (topography)	0.014	14	3.11	9292	0.68	0.25	0.0459
TI01	intermediate (topography)	0.014	14	6.70	20020	1.46	0.19	0.0430
TL01	lower (topography)	0.014	14	4.51	13476	0.98	0.38	0.0458
TL02	lower (topography)	0.008	8	4.25	12699	1.23	0.15	0.0457
TL03	lower (topography)	0.011	11	4.70	14044	1.16	0.14	0.0440
TL04	lower (topography)	0.018	18	5.10	15239	0.98	0.21	0.0451
TL05	lower (topography)	0.024	24	5.73	17121	0.95	0.22	0.0446

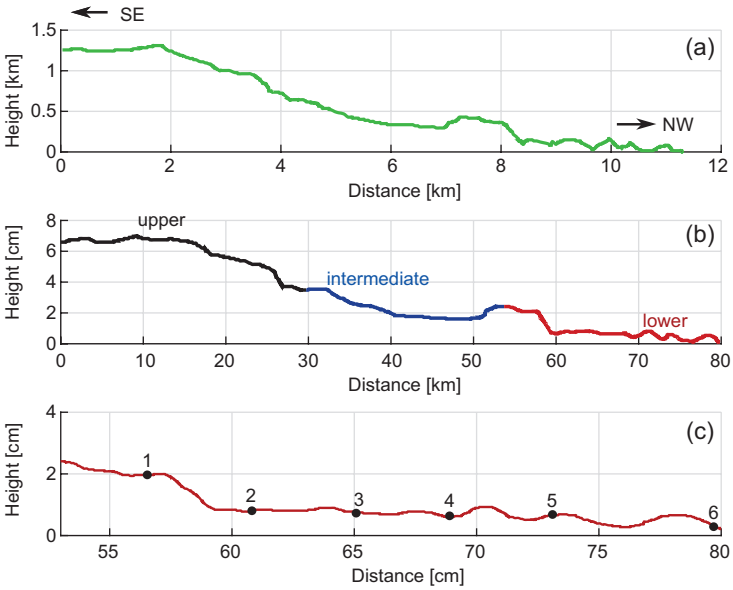

Fig. 1 (a) Height versus horizontal distance of the north-western (NW in the figure) side of the slope of the Tlaloc volcano. SE stands for the southeast. (b) The three different sections of the slope, upper (black), intermediate (blue), and lower (red), are shown. A detail of the testing slope, i.e., lower section (c), shows the location of the stations where the pressure time series are estimated. In all cases, the horizontal distance is measured from the beginning of the slope.

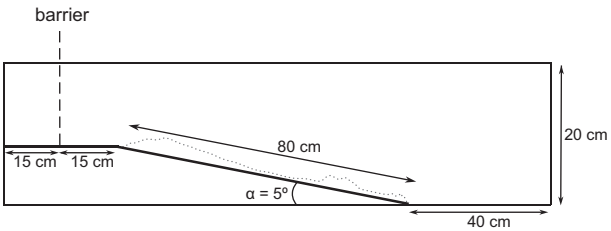

Fig. 2 Schematic of the experimental lock-release tank to generate the gravity currents. The overall dimensions of the tank were 150 × 20 × 7 cm; this last dimension (7cm) is not shown in the diagram for simplicity and because the GCs were studied in two dimensions.

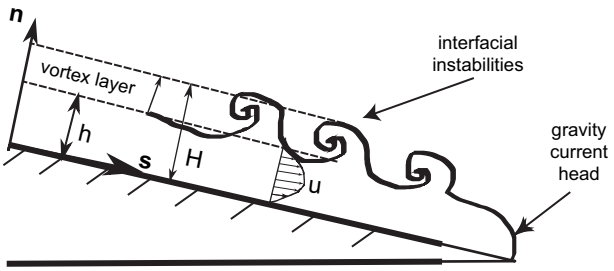

Fig. 3 Schematic representation of a gravity current in coordinates *s, n*, aligned with the slope, which is used to calculate the entrainment in the vortex layer ($H - h$). Sketch of the figure modified from Princevac et al. (2008).

For each gravity current, the height is represented with two values: H and h. The former (H) is the distance from the solid boundary to the interface between the current and its surroundings, taking into account the vortex layer; while h does not take this layer into account. The schematic representation for these variables is shown in figure 3. The vortex layer is the region where the entrainment occurs between the gravity current and its surroundings. The scale of the velocity U, parallel to the slope, is calculated from the PIV estimated velocity fields, considering the equation shown by Princevac et al. (2008):

$$U \cdot h = \int_0^H u \, dn \tag{6}$$

where u is calculated from the measured velocity fields, it is noteworthy to mention that the velocities are measured inside the gravity current domain at each time step in the direction of the slope. The characteristic velocity for entrainment, w_e, is rather difficult to be estimated from the experimental data (Wilson et al., 2017). Here, we developed a MATLAB code to estimate this w_e by directly using velocity fields and not from the area considerations proposed by previous authors (Ottolenghi et al., 2016; Nogueira et al., 2013; Wilson et al., 2017). To do so, we calculate the maximum values of vorticity in the s, n coordinates; then, we consider a small region around that maximum for each s and define that range as the vortex layer ($H - h$). This small region was estimated by the 5 pixels around the maximum vorticity pixel. Then, we look at the velocities inside this region (H − h) and the n component inside that vortex layer, which are considered the entrainment velocities w_e. For each instantaneous velocity field measurement, we estimate E using the mean values of U and w_e inside the gravity current for that velocity field. Then, for each gravity current, we get an entrainment time series (equation 5).

2.3 Pressure time series

Pressure fields are estimated from the velocity field measurements. An algorithm developed by Dabiri et al. (2014) that integrates the pressure gradient term from the Navier-Stokes equations is implemented for our study. This algorithm is contained in a MATLAB toolbox called *queen 2.0 Pressure Calculator* (Dabiri et al., 2014). From our instantaneous 2D velocity field estimates, we compute the corresponding instantaneous pressure fields, which are later used to generate the pressure time series at the stations shown in figure 1 (c). Once having those instantaneous pressure fields, we define synthetic stations along the topographic slope and calculate the pressure time series in each station. We obtain a set of six pressure time series for each gravity current propagating along the topographic slope.

3. Results

3.1 Velocity Fields

As the gravity currents propagated over the flat and topographic slopes, velocity fields were obtained with the PIV technique. Figure 4 shows these fields for three of the cases of gravity currents: F01 (flat slope), TU01 (upper topographic slope), and TL01 (lower topographic section). All these three cases correspond to $g' = 14$ cm s^{-2}; however, the velocity fields of these gravity currents show different structures, elucidating that the topography clearly impacts their propagation. Over the flat slope, higher velocities are reached, and they are uniform regardless of GC propagation. Moreover, the velocity reaches higher values as the GC evolves, showing a more rapid displacement at 5.45 and 7.27 s. Over the upper part of the topographic slope (TU01), as the head of the gravity current displaces over an irregular slope, higher velocities are reached in some zones of the GC compared with other zones; this becomes particularly clear at 5.45 and 7.27 s. Over the lower part of the topographic slope (TL01), non-uniform velocities also develop within the GC, and a clear vortex mixing layer is identified in the inter-phase between the GC and the ambient fluid.

3.2 Entrainment estimations

Entrainment is estimated for each GC as it propagates over the different sections of the slope. We compare the mean entrainment of each run and investigate the cases that resulted in higher entrainment and, therefore, more mixing. Entrainment time series are obtained to investigate how mixing processes occur while the gravity currents propagate. For each velocity field, E is calculated with the mean values of U and w_e; this last quantity is estimated from the velocities in the vortex layer following the procedure explained in section 2.2. We consider a dimensionless time $t = t / t_f$, where t is the current time, and t_f is the total time lapse. Figure 5 shows the entrainment E for two cases, with $g' = 14$ cm s^{-2}. One corresponds to a GC over the flat slope; the other is a selected GC in a topographic section (runs F01 and TL01). The rest of the results are summarized in figure 6.

The entrainment time series of figure 5 shows that E rapidly fluctuates in time and reaches its highest values in the first half of the time series. During this lapse, the head of the gravity current (and the vortex behind this head) are in the domain of study, i.e., in the section of the flow being recorded by the camera. A decreasing tendency appears at the end of the time series when the main vortices that enhance mixing are

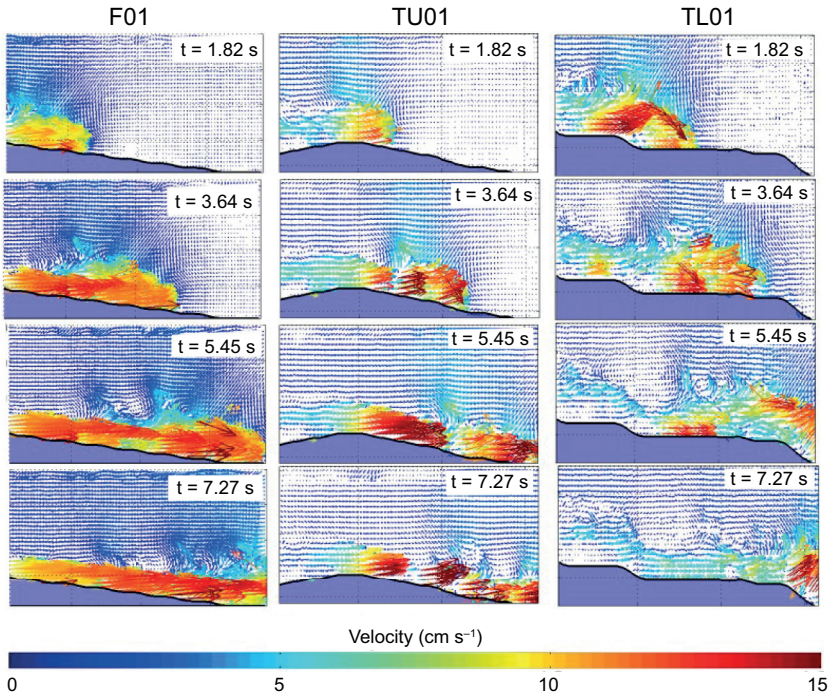

Fig. 4 Velocity fields obtained with PIV for GC over the flat slope (F01, left), upper topographic section (TU01, middle), and lower topographic section (TL01, right). In all these three cases, $g' = 14$ cms^{-2}; however, different structures for the velocity fields are seen for GCs depending on the bottom where they propagate.

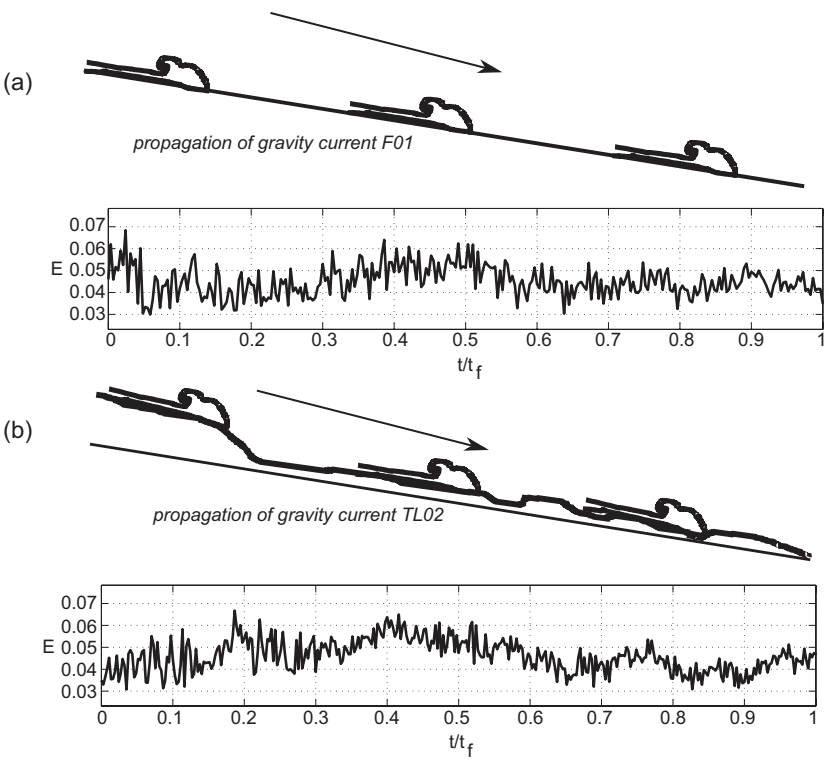

Fig. 5 Entrainment time series for the transit time of a GC to cross the observation domain for two cases: (a) GC over the flat slope and $g' = 14$ cms^{-2} (run F01) and (b) GC over the lower section of the synthetic topography with $g' = 14$ cms^{-2} (run TL01).

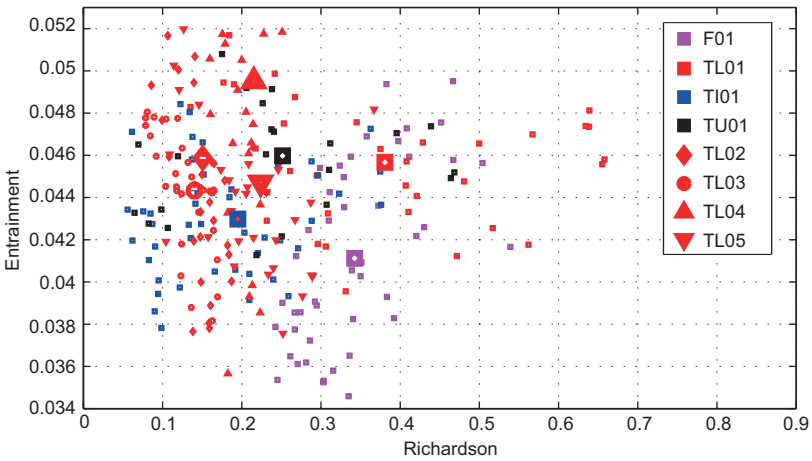

Fig. 6 Estimated entrainment coefficient as a function of the Richardson number for the eight runs of GC of Table I. The prominent solid symbols correspond to the mean values of each run. In contrast, spatial mean values, the small figures, are calculated corresponding to one centimeter of each current's displacement.

already out of the domain of study. As the GC flows over the slope, it dissipates energy over the rough topography and, therefore, also loses entrainment potential.

Entrainment values are small (on average 4.59×10^{-2} and 4.15×10^{-2} for TL01 and F01, respectively), and due to the turbulent nature of the vortex region defined for the entrainment calculation, it shows a large variability. Entrainment variability is slightly more considerable for the smooth topography experiment (F01), with variations representing 13.9% of the mean compared to 12.4% for the synthetic topography experiment (TL01). Amplitude spectra for these time series (Figure S3 in the supplementary material) show that energy is distributed among fewer frequencies in F01 than in TL01, which suggests that there is less variability of scales for the smooth case compared to the rough topography case.

Autocorrelation plots (Figure S4) show a weak positive autocorrelation for both time series, with correlation values of 0.2 or less for TL01 and between 0.4 and 0.2 for F01, although correlation values for the smooth case (F01) almost double those for the synthetic topography (TL01) for the first seven lag values (between 0.18 and 1.26 s). Autocorrelation decreases as the lag increases for the smooth case, which reflects the fact that E has a linear trend and declines in time (Fig. 5a). This is not the case for the rough topography GC, for which correlations are immediately smaller and increase noisily to a maximum correlation of 0.3 at lag 12.

We estimate the Richardson number (equation 4) for each instantaneous velocity field. We use fixed values of $d\rho / dz$ corresponding to Table I. A mean Richardson number (Ri) is calculated for each GC run. Figure 6 shows the relation between E and Ri. All the data points are added in figure 6, comparing all the experiments in Table I. A general trend indicates that the Richardson numbers are smaller for the synthetic topography, conversely with the flat cases with higher values. The lower the Ri, the higher the mixing; therefore, it appears that the topographic irregularities on the slope contribute to enhancing mixing.

Figure 6 shows that the lowest values of entrainment correspond to the flat slope (run F01, purple squares in the figure). Although this run has the highest velocity (and therefore the highest Reynolds number), the entrainment remains the lowest (E_{mean} = 0.0406), and the Richardson number in this gravity current reaches high values compared with the Ri corresponding to the GCs over the topographic slope. The intermediate section of the topographic bottom is the flattest one of this topography (see

figure 1). In this case, E is also low ($E_{mean} = 0.0430$) compared with the values of E reached in the upper ($E_{mean} = 0.0459$) and lower ($E_{mean} = 0.0458$) sections of the topographic slope. These different values of E, corresponding to all the experimentally studied gravity currents, are presented in figure 6. The increase in irregularities along the topographic surface appears to be related to higher entrainment values. Although the highest velocities (and highest *Re*) correspond to the flat slope, it suggests that the Re and the irregularities on the bottom contribute to the mixing between the gravity currents and the ambient fluid. The relation between the initial density contrast and the entrainment values is insufficient to elucidate a clear relationship between the g' and the entrainment. The highest values of E correspond to the gravity current with $g' = 18$ cm s^{-2} propagating over the lower section of the topography; in that case, $E \approx 0.049$. Nevertheless, smaller and larger density contrasts ($g' = 11$ cm s^{-2} and $g' = 24$ cm s^{-2}) are used in the same section with a very similar mean result for entrainment values ($E \approx 0.045$ for both values of g'), as can be seen in figure 6 and on Table I.

3.3 Pressure time series

The analysis of pressure time series allowed us to conceive a method for identifying gravity currents in the slope of mountains. We compute the time series from the pressure field estimates at the stations shown in figure 1 (c). Six pressure time series are obtained for each gravity current run in the lower section of the topographic profile. These six series correspond to each synthetic station shown in figure 1 (c). One set of time series (corresponding to the run TL01) is shown in figure 7, where higher frequency pressure fluctuations start successively as the GC reaches the stations. The GC arrived at station 1 before we started recording because pressure fluctuations have started since the beginning of the time series on that station. However, from stations 2 to 6, almost no pressure variations are seen at the beginning of the time series. Higher frequency variations are seen at successive times: At ≈ 0.8 s in station 2, at ≈ 1.6 s in station 3, at ≈ 2.8 s in station 4, at ≈ 3.8 s in station 5, and at ≈ 4.6 s in station 6. Similar behavior is observed in the pressure time series for all the runs. Additionally, we perform numerical test simulations, shown in the

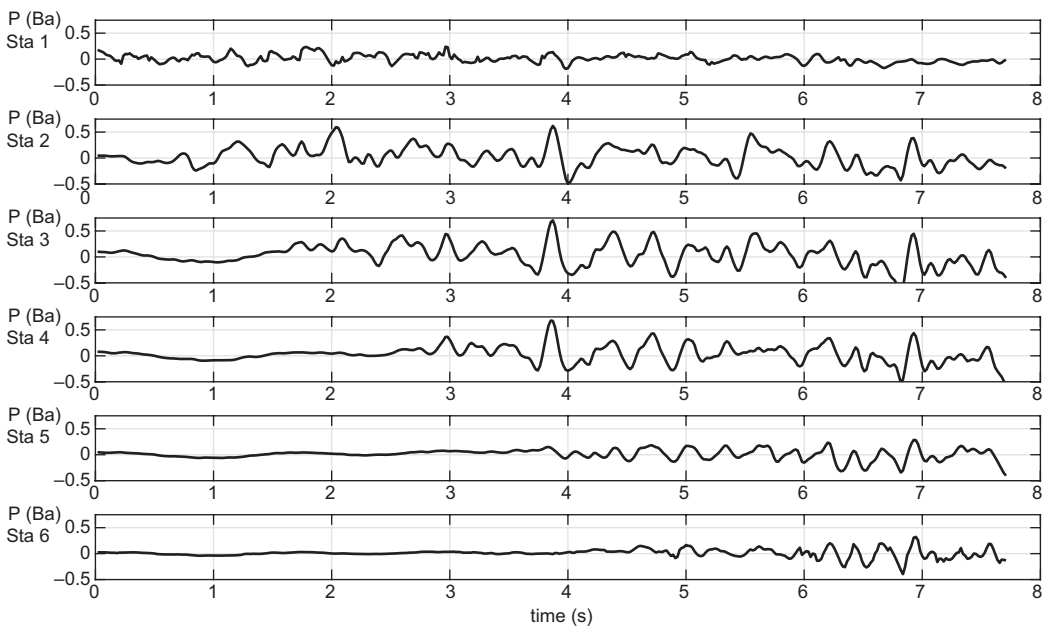

Fig. 7 Pressure time series in six synthetic stations in the lowest section of the topographic slope, run TL01. The upper panels correspond to the upstream stations showing higher fluctuations as the GC first appears and the fluctuations associated with the transit.

supplementary material, that corroborate this behavior qualitatively but support the existence of surface pressure variations as the gravity currents flow.

In addition, figure 7 shows similar pressure variations just before 4 seconds in stations 2, 3, and 4. This fast and high amplitude (≈ 0.5 Ba) pressure variation could be explained in terms of a hydraulic jump. The average Froude number in this particular gravity current (TL01), Fr =0.98, is very close to the critical value (Fr =1), and the pressure signal is similar to the one presented by previous authors in the suitable conditions for hydraulic jumps to develop (De Padova et al., 2018). However, further investigation is necessary to rigorously confirm the existence of a hydraulic jump in gravity current TL01.

More significant variability and energy in stations 2, 3, and 4 can also be confirmed from their standard deviations (0.19, 0. 23, 0.19 Ba, respectively) compared to stations 1, 5, and 6 (0.08, 0.12, 0.11 Ba, respectively), and greater power spectral density in amplitude spectra (Fig. S5 in supplementary material).

3.3 Qualitative flow visualization

The GCs are visualized to qualitatively characterize their shape and observe the structures that lead to mixing. This section presents visualizations of GCs with the lowest (TL02) and highest (TL05) density contrasts. The images in this subsection belong to runs TU01, TL02, and TL05. Figure 8 (a) shows a snapshot of a GC corresponding to run TU01. This photograph was taken using red light and dark ink. Clearly, a Kelvin-Helmholtz instability is formed at the interface. These instabilities are associated with mixing enhancement between the GC and the ambient fluid (Strang and Fernando, 2001). Shadowgraph visualizations are shown in Figures 8 (b) and (c), where the main structures of the gravity current's head, tail, and vortex can be seen behind them. Two sets of snapshots, corresponding to gravity currents with different g' in the lower section of the topographic slope, are shown. The set of snapshots of Figure 8 (b) corresponds to the largest $g' = 24$ cm s^{-2} (run TL05), and the right panels (c) correspond to the smallest density contrast: $g' = 8$ cm s^{-2} (run TL02); thus, a fainter shadow and light contrast can be seen when compared with the left panels. This behavior can be attributed to the fact that, in the shadowgraph technique, smaller contrasts of lights and shadows correspond to smaller density gradients (Panigrahi and Muralidhar, 2012).

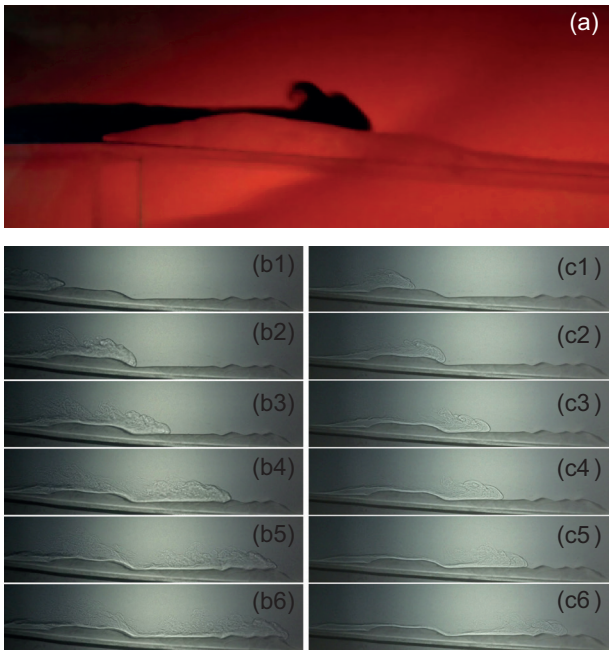

Fig. 8 Experimental GC visualizations for (a): Visualization with dark ink and red light of the TU01 gravity current propagating over the upper section of the topographic surface. (b) and (c): Snapshots of gravity currents propagating over the lower section of the topographic surface. On the left b1)-b6): a gravity current of the TL05 run ($g' = 24$ cm s^{-2}) is shown. On the right: c1)-c6): a gravity current of the TL02 run is shown, corresponding to $g' = 8$ cm s^{-2}.

In addition, in the visualization corresponding to run TL02, the vortices have more defined boundaries with sharp edges. In comparison, more mixing appears to form in run TL05, where the vortices are more diffuse. Additionally, we are interested in visualizing the propagation of the gravity currents as they interact with the irregularities of the topography. For both currents, when the head of these currents is traveling upwards in a topographical irregularity (Figure 8 b1, c1, and b5), it appears to be more defined, and fewer vortices are visible. When the currents travel downwards over a topographical irregularity, more vortices and contrasts of shadows and lights result (Figure 8 b3, b4, c3, and c4), suggesting that mixing may increase.

4. Conclusions

In this study, we investigated experimentally downsloping gravity currents over varying synthetic topography, along which we identified and characterized the enhanced mixing regions by using the temporal and spatial variability of the entrainment coefficient, E. The synthetic topography is a simplified scaled profile analogous to one on the hillside of a real mountain, which, to the best of our knowledge, has yet to be experimentally studied with the PIV techniques presented in this investigation. We used the entrainment coefficient as a proxy for the development of the mixing between the gravity current and the ambient fluid based on previous definitions adapted for our PIV experiment measurements and a non-flat slope (see Methods). We perform several experiments with different density contrasts, and we find that the entrainment consistently increases as the roughness of the topographic bottom increases. The lowest values of E are found for the flat slope experiment (F01) ($E_{mean} = 0.041$) and for the intermediate (and flattest) section of the synthetic hillside-like-topography ($E_{mean} = 0.043$). For a given density contrast ($g' = 14$ cm s^{-2}), the highest values of E correspond to the upper and lower sections of the topography ($E_{mean} = 0.0459$ and $E_{mean} = 0.458$ respectively), corresponding to the regions where the roughness increases. While we observe a dependence of E with the slope roughness, we did not find any clear dependence between the density contrast and the entrainment values. The dependence between E and the roughness may also be qualitatively identified in the shadowgraph images in figure 8, where more mixing occurs when the gravity currents propagate over the irregularities of the slope.

From the velocity fields obtained with the PIV, we derived the pressure fields, which represent our second quantitative analysis. For the six synthetic stations on the lower section of the topographic slope, we analyze the pressure time series showing that the arrival of the gravity current can be observed. High-frequency variations in pressure arise as the current propagates over the synthetic stations, suggesting that this analysis can be implemented for real atmospheric gravity currents at particular locations of mountain slopes. Gravity currents in the atmosphere usually have much more complex dynamics than in experiments. However, these experimental models help understand the most basic underlying dynamics of real geophysical flows. The present study contributes to this understanding by considering a more realistic synthetic topography and its influence on mixing processes. In addition, the signal of the pressure time series we found is a novel aspect in analyzing experimental gravity currents. Its applicability in thermally driven winds on the slope of mountains should be further investigated in future research.

Acknowledgments

We thank CONACyT (Consejo Nacional de Ciencia y Tecnología) for providing financial support to pursue the master's studies of A. Burgos-Cuevas.

References

Adduce C, Sciortino G, Proietti S. 2012. Gravity Currents Produced by Lock Exchanges: Experiments and Simula-tions with a Two-Layer Shallow-Water Model with Entrainment. Journal of Hydraulic Engineering, 138: 111–121. https://doi.org/10.1061/(ASCE)HY.1943-7900.0000484

Aiki H, Yamagata T. 2004. A numerical study on the successive formation of Meddy-like lenses. Journal of Geophysical Research: Oceans, 109: C6. https://doi.org/10.1029/2003JC001952

Balasubramanian S, Zhong Q. 2018. Entrainment and mixing in lock-exchange gravity currents using simultaneous velocity-density measurements. Physics of Fluids 30: 056601. https://doi.org/10.1063/1.5023033

Benjamin TB. 1968. Gravity currents and related phenomena. Journal of Fluid Mechanics 31: 209-248. https://doi.org/10.1017/S0022112068000133

Bhaganagar K, Pillalamarri NR. 2017. Lock-exchange release density currents over three-dimensional regular roughness elements. Journal of Fluid Mechanics 832: 793-824. https://doi.org/10.1017/jfm.2017.678

Cenedese C, Nokes R, Hyatt J. 2016. Mixing in a density-driven current flowing over a rough bottom. In 20th Australasian Fluid Mechanics Conference, Perth, Australia.

Cenedese C, Nokes R, Hyatt J. 2018. Lock-exchange gravity currents over rough bottoms. Environmental Fluid Mechanics 18: 59-73. https://doi.org/10.1007/s10652-016-9501-0

Cenedese C, Adduce C. 2008. Mixing in a density-driven current flowing down a slope in a rotating fluid. Journal of Fluid Mechanics 604: 369-388. https://doi.org/10.1017/S0022112008001237

Dabiri JO, Bose S, Gemmell BJ, Colin SP, Costello JH. 2014. An algorithm to estimate unsteady and quasi-steady pressure fields from velocity field measurements. Journal of Experimental Biology 217: 331-336. https://doi.org/10.1242/jeb.092767

De Falco MC, Adduce C, Maggi, MR. 2021. Gravity currents interacting with a bottom triangular obstacle and implications on entrainment. Advances in Water Resources 154: 103967. https://doi.org/10.1016/j.advwatres.2021.103967

De Padova D, Mossa M, Sibilla S. 2018. SPH numerical investigation of characteristics of hydraulic jumps. Environmental Fluid Mechanics 18: 849-870. https://doi.org/10.1007/s10652-017-9566-4

Doran, JC, Abbott S, Archuleta J, Bian X, Chow J, Coulter RL, de Wekker SFJ, Edgerton S, Elliott S, Fernandez A, Fast JD, Hubbe JM, King C, Langley D, Leach J, Lee JT, Martin TJ, Martinez D, Martinez JL, Mercado G, Mora V, Mulhearn M, Pena JL, Petty R, Porch W, Russell C, Salas R, Shannon JD, Shaw WJ, Sosa G, Tellier L, Templeman B, Watson JG, White R, Whiteman CD, Wolfe D. 1998. The IMADA-AVER Boundary Layer Experiment in the Mexico City Area. Bulletin of the American Meteorological Society 79: 2497-2508. https://doi.org/10.1175/1520-0477(1998)079<2497:TIABLE>2.0.CO;2

Ellison TH, Turner JS, 1959. Turbulent entrainment in stratified flows. Journal of Fluid Mechanics 6: 423-448. https://doi.org/10.1017/S0022112059000738

Fast JD, Zhong S. 1998. Meteorological factors associated with inhomogeneous ozone concentrations within the Mexico City basin. Journal of Geophysical Research: Atmospheres 103: 18927–18946. https://doi.org/10.1029/98JD01725

Fleischmann CM, Pagni PJ, Williamson RB. 1994. Saltwater Modeling Of Fire Compartment Gravity Currents. Fire Safety Science 4: 253–264. http://doi.org/10.3801/IAFSS.FSS.4-253

Huppert HE, Simpson JE. 1980. The slumping of gravity currents. Journal of Fluid Mechanics 99: 785-799. https://doi.org/10.1017/S0022112080000894

Linden P. 2012. Gravity currents-theory and laboratory experiments. In: Chassignet EP, Cenedese C, Verron J, eds. Buoyancy Driven Flows. Cambridge: Cambridge University Press, pp. 13-51. https://doi.org/10.1017/CBO9780511920196.002

Jiang Y, Liu X. 2018. Experimental and numerical investigation of density current over macro-roughness. Environmental Fluid Mechanics 18: 97-116. https://doi.org/10.1007/s10652-016-9500-1

Lowe RJ, Linden P, Rottman JW. 2002. A laboratory study of the velocity structure in an intrusive gravity current. Journal of Fluid Mechanics, 456: 33-48. https://doi.org/10.1017/S0022112001007303

Maggi MR, Adduce C, Negretti ME. 2022. Lock-release gravity currents propagating over roughness elements. Environmental Fluid Mechanics 22: 383–402. https://doi.org/10.1007/s10652-022-09845-6

Manins PC, Sawford BL. 1979. A Model of Ktabatic Winds. Journal of the Atmospheric Sciences 36: 619–630. https://doi.org/10.1175/1520-0469(1979)036<0619:AMOKW>2.0.CO;2

Marshall J, Hill C, Perelman L, Adcroft A. 1997. Hydrostatic, quasi-hydrostatic, and nonhydrostatic ocean modeling. Journal of Geophysical Research: Oceans 102: 5733–5752. https://doi.org/10.1029/96JC02776

Mitsudera H, Baines PG. 1992. Downslope gravity currents in a continuously stratified environment: A model of the bass strait outflow. In: Proceedings of the 11th Australasian Fluid Mechanics Conference. Hobart, Australia. 1017–1020.

Mukherjee P, Balasubramanian S. 2020. Energetics and mixing efficiency of lock-exchange gravity currents using simultaneous velocity and density fields. Physical Review Fluids 5: 063802. https://doi.org/10.1103/PhysRevFluids.5.063802

Mukherjee P, Balasubramanian S. 2021. Diapycnal mixing efficiency in lock-exchange gravity currents. Physical Review Fluids 6: 013801. https://doi.org/10.1103/PhysRevFluids.6.013801

García-Molina C. 2020. Lee waves and wake generated by a steady current passing over a spherical cap, comparing linear, numerical and experimental approaches. Doctoral thesis, Université Grenoble Alpes.

Nogueira HI, Adduce C, Alves E, Franca MJ. 2013. Analysis of lock-exchange gravity currents over smooth and rough beds. Journal of Hydraulic Research 51: 417–431. https://doi.org/10.1080/00221686.2013.798363

Nogueira HIS, Adduce C, Alves E, Franca MJ. 2014. Dynamics of the head of gravity currents. Environmental Fluid Mechanics 14: 519–540. https://doi.org/10.1007/s10652-013-9315-2

Ottolenghi L, Adduce C, Inghilesi R, Roman F, Armenio, V. 2016. Mixing in lock-release gravity currents propagating up a slope. Physics of Fluids 28: 056604 https://doi.org/10.1063/1.4948760

Ottolenghi L, Cenedese C, Adduce C. 2017. Entrainment in a Dense Current Flowing Down a Rough Sloping Bottom in a Rotating Fluid. Journal of Physical Oceanography 47: 485-498. https://doi.org/10.1175/JPO-D-16-0175.1

Panigrahi PK, Muralidhar K. 2012. Schlieren and Shadowgraph Methods in Heat and Mass Transfer. New York: Springer New York. https://doi.org/10.1007/978-1-4614-4535-7

Princevac M, Hunt JCR, Fernando HJS. 2008. Quasi-Steady Katabatic Winds on Slopes in Wide Valleys: Hydraulic Theory and Observations. Journal of the Atmospheric Sciences 65: 627–643. https://doi.org/10.1175/2007JAS2110.1

Reuten C, Steyn DG, Allen SE. 2010. Upslope Flows in Atmosphere and Water Tank, Part II: Fluid-Dynamical Smoothness as a Possible Cause for Velocity Similarity Violation. The Open Atmospheric Science Journal 4: 188-201. https://doi.org/10.2174/1874282301004010188

Shin JO, Dalziel SB, Linden PF. 2004. Gravity currents produced by lock exchange. Journal of Fluid Mechanics 521: 1–34. https://doi.org/10.1017/S002211200400165X

Simpson JE. 1999. Gravity currents in the environment and the laboratory. Cambridge University Press.

Strang EJ, Fernando HJS. 2001. Entrainment and mixing in stratified shear flows. Journal of Fluid Mechanics 428: 349–386. https://doi.org/10.1017/S0022112000002706

Tanino Y, Nepf HM, Kulis PS. 2005. Gravity currents in aquatic canopies. Water Resources Research 41: W12402. https://doi.org/10.1029/2005WR004216

Tokyay T, Constantinescu G. 2015. The effects of a submerged non-erodible triangular obstacle on bottom propagating gravity currents. Physics of fluids 27: 056601. https://doi.org/10.1063/1.4919384

Turner JS. 1986. Turbulent entrainment: the development of the entrainment assumption, and its application to geophysical flows. Journal of Fluid Mechanics 173: 431–471. https://doi.org/10.1017/S0022112086001222

Ungarish M. 2009. An introduction to gravity currents and intrusions. New York: CRC Press. https://doi.org/10.1201/9781584889045

Ungarish M. 2016. On the front conditions for gravity currents in channels of general cross-section. Environmental Fluid Mechanics 16: 747-775. https://doi.org/10.1007/s10652-015-9443-y

Wilson RI, Friedrich H, Stevens C. 2017. Turbulent entrainment in sediment-laden flows interacting with an obstacle. Physics of Fluids 29: 036603. https://doi.org/10.1063/1.4979067

Wu C-S, Dai A. 2020. Experiments on two-layer stratified gravity currents in the slumping phase. Journal of Hydraulic Research 58: 831–844. https://doi.org/10.1080/00221686.2019.1671517

Xu S, Liu N, Yan J. 2019. Residual-based variational multi-scale modeling for particle-laden gravity currents over flat and triangular wavy terrains. Computers & Fluids 188: 114–124. https://doi.org/10.1016/j.compfluid.2019.05.008

Zhang X, Nepf HM. 2008. Density-driven exchange flow between open water and an aquatic canopy. Water Resources Research 44: W08417 https://doi.org/10.1029/2007WR006676

Zhou J, Venayagamoorthy SK. 2020. Impact of ambient stable stratification on gravity currents propagating over a submerged canopy. Journal of Fluid Mechanics 898: A15. https://doi.org/10.1017/jfm.2020.418

Supplementary Material

1. Numerical simulation of lock-exchange gravity currents

In this section, we present the results of a set of numerical simulations performed to reproduce, as similar as possible, the gravity currents (GC) that propagate in the laboratory-developed setup. Two-dimensional gravity currents traveling downslope over the same topographic bottom as in the experimental case are simulated. These simulations aim to support the structure and some quantities. Thus, the entrainment and other variables are not estimated. Nevertheless, in this section, we provide a visualization of the GCs, and as in the experimental case, we include the pressure time series.

1.1 Numerical set-up

We perform numerical simulations with boundary conditions corresponding to experimental GCs propagating over the lower section of the topographic slope (TL01, TL02, TL03, TL04, and TL05). We run these simulations using the Non-hydrostatic Ocean Model for the Earth Simulator (NHOES). This model was written in FORTRAN 90 by Hidenori Aiki (Aiki and Yamagata, 2004). It has two available versions: Non-hydrostatic Model (NHM) and Non-hydrostatic Rectangular Model (NHRM). In the present work, we use the NHRM version. The basic formulation of the model is based on Marshall et al. (1997) non-hydrostatic, incompressible Boussinesq equations discretized with Arakawa's C-grid. This numerical model employs the Smagorinsky turbulence parametrization and a leap-frog time step scheme. It has some differences with MITgcm, as it is further explained by García-Molina (2020). We use a regularly spaced grid with a spatial resolution of 2.5 mm along the x- and y-directions. To assure the convergence of the model, the time step is set to $\delta t = 1 \times 10^{-4}$ s. For all cases, we impose closed and free-slip boundary conditions.

Similarly to the experimental setup, a flat horizontal surface of 30 cm in length is imposed on the left of the physical domain. The viscosity of the fluid is set to be $\nu = 10^{-2}$ cm^{-2} s^{-1} and the diffusivity is set to 10^{-5} cm^2 s^{-1}. The system's initial condition sets a non-equilibrium configuration, which induces a GC via an anomaly in the density profile of the fluid. This anomaly in density only exists before reaching the physical domain at x = 0 cm, and it is set as follows: From x = −30 cm to x = −15 cm, a fluid column of density is imposed. For x > −15 cm, the density of the fluid is smaller (ρ_0), such that $\rho_0 < \rho_1$.

The higher density (ρ_1) is set accordingly to each of the experimental cases in the lower section of the topography (TL01, TL02, TL03, TL04, and TL05). Gravity is imposed as an external forcing along the vertical direction, and the numerical GCs are allowed to propagate 30 cm horizontally before they travel downslope.

Thus, as we did in the experimental setup, this density anomaly constitutes only a mechanism to develop a GC before reaching the slope.

Figure 9 shows the numerical visualizations of the density fields of GCs. All the density contrasts utilized for the experimental GCs in the lower section of the topography are also visualized numerically (runs TL01-TL05). Clearly defined fronts followed by a set of KH's instabilities are visible in the numerical visualizations. These instabilities lead to mixing behind the GC front, resulting in a density distribution between $\rho_0 = 1000$ kgm^{-3} and $\rho_1 = 1008$ kgm^{-3}, $\rho_1 = 1011$ kgm^{-3}, $\rho_1 = 1014$ kgm^{-3}, $\rho_1 = 1024$ kgm^{-3} for (a), (b), (c), (d), and (e) respectively. This figure provides a density visualization and not a quantitative mixing parameter, partly because of that, it is not possible to elucidate stronger mixing for some density contrasts rather than others. However, the lack of a clear dependence between the density contrast and mixing is coincident with the fact that, in the experimental GCs, the entrainment did not show a clear dependence with g' neither.

1.2 Numerical pressure time series

The same pressure stations as in the experimental GCs are defined, and we estimate the pressure time series in those stations. Figure S2 shows these numerical pressure time series, where the arrival of the GC is detected as a pressure variation. Similarly to the experimental case, these variations start at subsequent times in each station. Nevertheless, the numerical pressure variations have high amplitudes but lower frequencies than the experimental ones. Additionally, these numerical pressure variations dampen faster than the experimental ones. Only the subsequent initial pressure perturbation identifies the arrival of the numerical GC to the synthetic stations along the slope, as in the experimental case.

2. Time series analysis

2.1 Entrainment

Power spectral density (PSD) in the lower frequencies, between 2 and 9 Hz (Fig. S3 shaded area), is distributed similarly for both smooth and rough topographies, while energy is not distributed equally at higher frequencies. The most prominent peak for the synthetic topography spectra is at 28 Hz, while the most prominent peak for the smooth case is at 9.4 Hz.

Energy is distributed among fewer frequencies in the smooth case (fewer peaks for F01 than for TL01), which confirms less variability of scales for the smooth case compared to the rough topography.

Autocorrelation plots (Fig. S4) show a weak positive autocorrelation for both time series (0.2 or less for TL01 and between 0.4 and 0.2 for F01), although correlation values for the smooth case (F01) are almost double those for the synthetic topography (TL01) for the first seven lag values (between 0.18 and 1.26 s). Autocorrelation decreases as the lag increases for the smooth case for lags smaller than 14. The fact that autocorrelation decreases for the smooth case means that E has a linear trend and declines in time, which can be seen from the time series. This is not the case for the rough topography case, for which correlations are immediately smaller and increase noisily to a maximum correlation of 0.3 at lag 12.

2.2 Pressure

Power spectral density for pressure at all stations (Fig. S5) shows more energy, seen as taller peaks at stations 2, 3, and 4. This agrees with having larger variability at those stations, evident from time series plots with larger standard deviations.

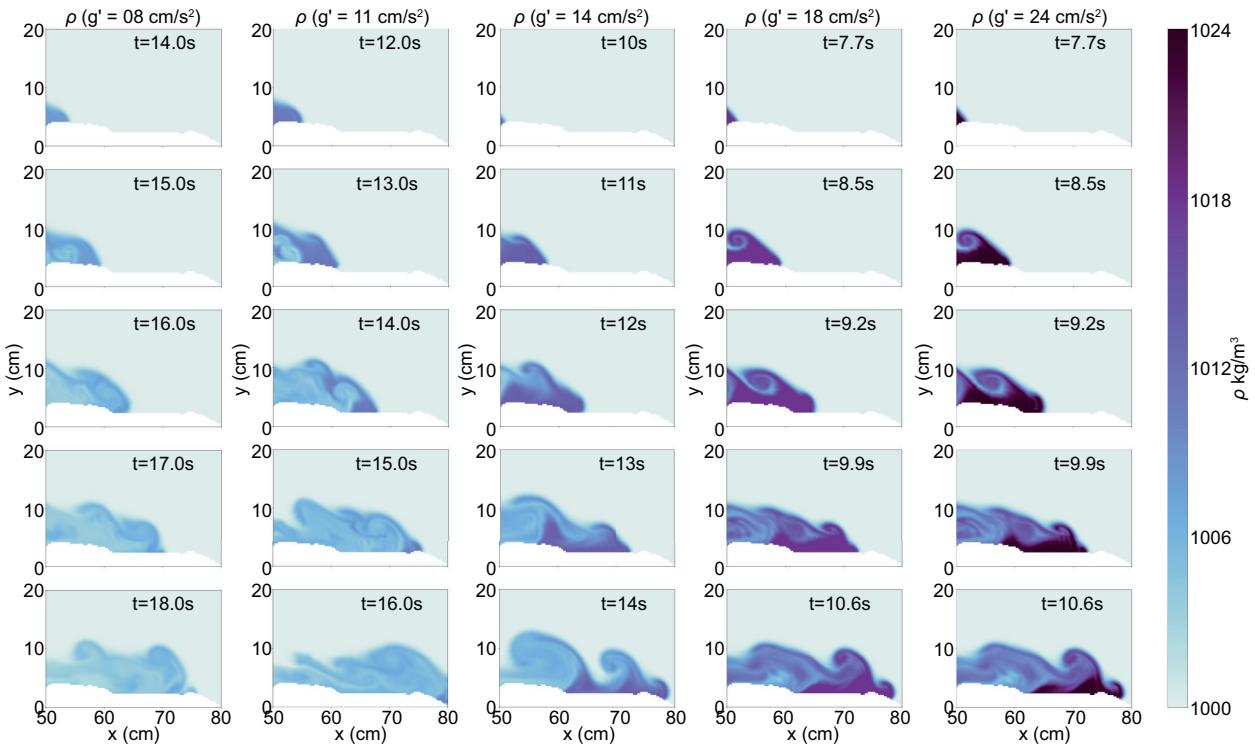

Fig. S1 Density fields visualization of the GCs propagating over the lower section of the topographic slope with varying density contrasts: (a) $g' = 8\text{cms}^{-2}$ (TL02), (b) $g' = 11\text{cms}^{-2}$ (TL03), (c) $g' = 14\text{cms}^{-2}$ (TL01), (d) $g' = 18\text{cms}^{-2}$ (TL04), and (e) $g' = 24\text{cms}^{-2}$ (TL05).

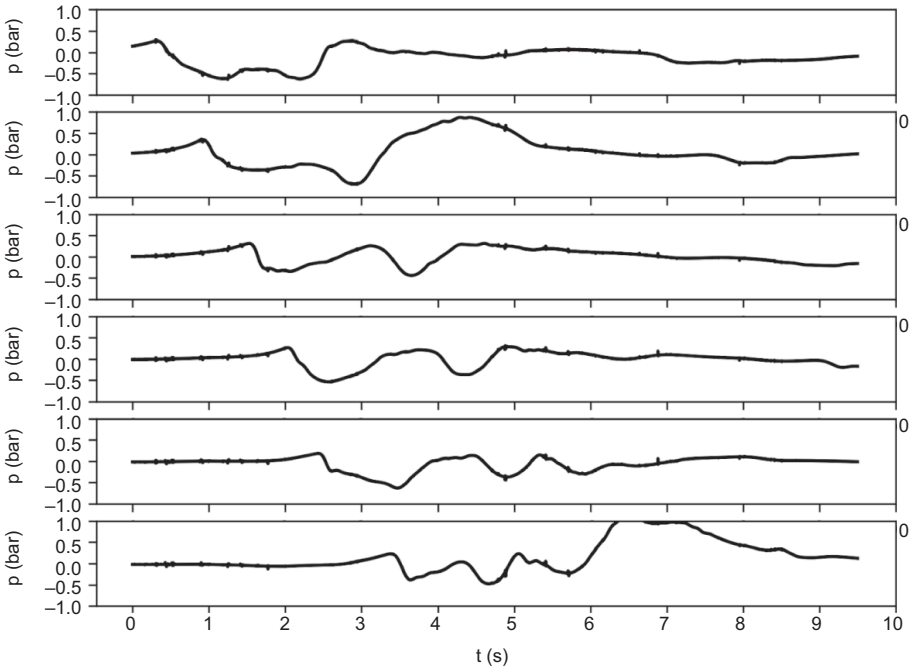

Fig. S2 Numerical pressure time series in six synthetic stations in the lowest section of the topographic slope, run TL01.

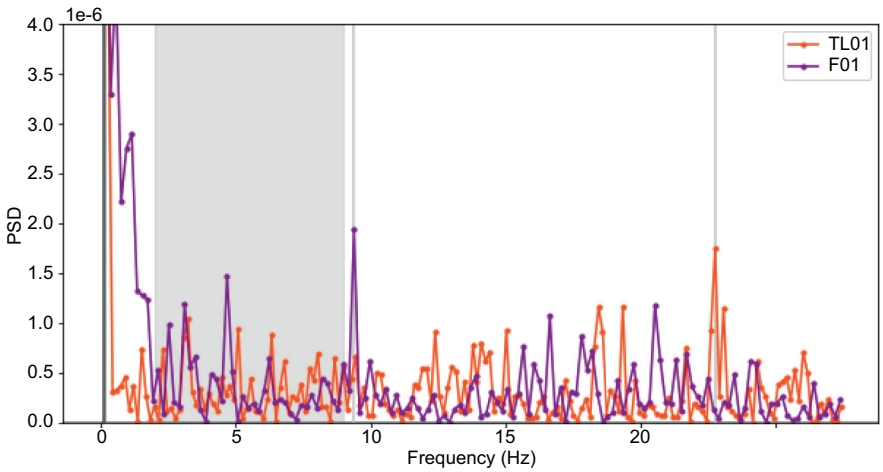

Fig. S3 Amplitude spectra for the smooth and synthetic topographies. Prominent peaks close to zero frequency correspond to the length of the time series and should be ignored.

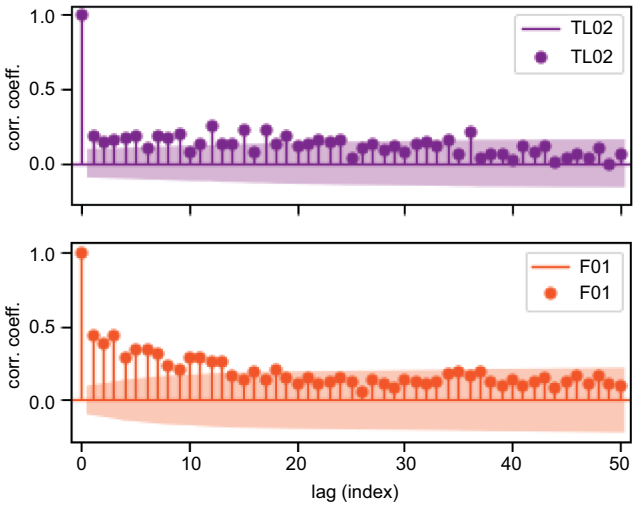

Fig. S4 The y-axis shows the correlation coefficient between the original time series and the same time series moved by a particular lag value (dots). The lag index is equivalent to a time lag of index*dt where dt is approximately 1/55 Hz (0.18 sec). Positive values indicate a positive correlation, and negative values indicate a negative correlation. Note that there is a 100% positive correlation when the lag=0 (r=1) since we are just comparing the time series to itself. The shaded area is the confidence interval with a default value of $\alpha = 0.05$ (95% confidence interval). Anything within this range represents a value that has no significant correlation with the most recent value of E.

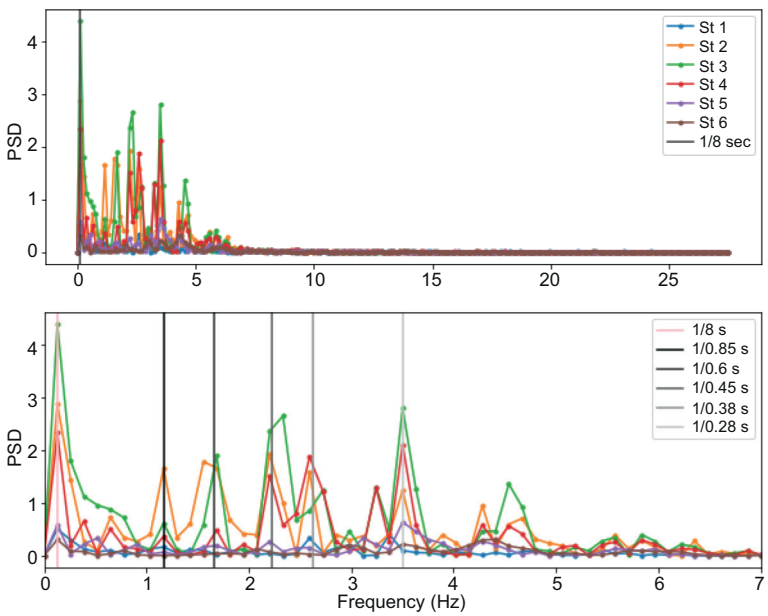

Fig. S5 Amplitude spectra for pressure at all stations. The prominent peak at a frequency of ⅛ s corresponds to the length of the time series and should be ignored.